CHAPTER 3
PREDICTION OF PRISTINE C_{18} NANOCLUSTER AS A HAZARDOUS GAS SENSOR

3.1. INTRODUCTION

In Chapter 1, the thesis highlighted the severe health risks associated with hazardous gases like CO, NO, and NH_3. These gases, often produced from improper burning of fossil fuels, pose significant dangers to both the environment and human health. CO and NO, being colourless and odourless, are particularly dangerous, leading to potential fatalities due to unconsciousness or severe respiratory issues upon exposure [1-2]. NH_3, although widely used in various applications, can also cause significant health issues in concentrated forms, including skin, eye, and lung irritation.

Given these risks, the need for reliable gas detection technologies has surged, prompting extensive research into various carbon allotropes like graphene, carbon nanotubes, and unique structures like cyclo[18]carbon (C_{18}). Recent studies have shown promising gas adsorption capabilities of these allotropes, especially when doped or functionalized with specific elements. For instance, graphene's interaction with CO gas changed when aluminium was introduced, altering adsorption behaviour from physical to chemical bonding [3-16].

Numerous studies exploring the gas adsorption behaviours of various carbon allotropes, their interactions with different hazardous gases, and the significant enhancements brought about by element doping. These investigations demonstrate the potential for creating highly sensitive and responsive gas sensors [17-23]. Despite this progress, the present chapter emphasizes the underexplored potential of C_{18} nanoclusters in gas sensing applications. Previous studies have examined the structural and electronic properties of C_{18}, showcasing its unique characteristics as a semiconductor and its potential application in molecular machines and nano-mechanical systems [23-29]. However, research regarding its gas adsorption capabilities, especially concerning hazardous gases like CO, NO, and NH_3, remains scarce.

Building on existing insights, the thesis aims to fill this research gap by investigating the adsorption behaviour of hazardous gases on C_{18} nanoclusters using a first-principles approach rooted in density functional theory [30-31]. The study intends to explore not only the adsorption characteristics but also the structural, electronic, absorption, and vibrational properties of both pristine C_{18} nanoclusters and those interacting with hazardous gas molecules. This exploration seeks to unveil the potential of C_{18} nanoclusters as effective and responsive sensors for hazardous gases.

3.2. METHODOLOGY

The investigation involved employing first-principles density functional theory (DFT) calculations with the Gaussian 09 package [32]. For optimizing the C_{18} nanocluster, we opted for the range-separated hybrid ωB97XD, known for accurately replicating the experimentally observed structural geometry of polyynic C_{18} [24-25, 33]. All geometry optimizations were carried out using the 6-311++G(d, p) Gaussian basis set [25]. We applied the same theoretical framework to compute total energies, electronic characteristics, molecular electrostatic potential (MEP), density of states (DOS), global index parameters, work function, relaxation time, and adsorption energies. Utilizing the outcomes of the density functional theory (DFT) calculations, the structural geometry, molecular orbitals, Mulliken charges, and MEP were visually represented using GaussView (version 6) [34]. Density of states (DOS) plots were generated using GaussSum software [35]. The calculation process adhered to specific convergence criteria: 12×10^{-4} radian for the root-mean-square (rms) displacement gradients, 18×10^{-4} Bohr for maximum displacement, 3×10^{-4} Hartree/radian for rms force, and 45×10^{-5} Hartree/Bohr for maximum force. The HOMO-LUMO gap (E_G), defined as the disparity between the highest occupied molecular orbital (HOMO) and the lowest unoccupied molecular orbital (LUMO) [36-38], is expressed as:

$$E_G = E_{LUMO} - E_{HOMO} \text{ ----- (1)}$$

Here, E_{LUMO} represents the energy of the lowest unoccupied molecular orbital (LUMO), and E_{HOMO} corresponds to the energy of the highest occupied molecular orbital (HOMO). The Fermi level energy (E_F) [36, 38-39] is determined by the following relationship:

$$E_F = (E_{LUMO} + E_{HOMO})/2 \text{ ------ (2)}$$

3.3. RESULTS AND DISCUSSION

3.3.1. Structural and electronic properties of pristine C_{18} nanocluster

Before investigating how hazardous gas molecules NO, CO, and NH_3 interact with the C_{18} nanocluster, we optimized its structure using the ωB97XD/6-311++G(d, p) theory level. The optimized structure, shown in Fig. 1(a), demonstrates lengths for single (C-C) and triple (C≡C) carbon-carbon bonds at 1.34 Å and 1.22 Å, respectively, indicating sp-sp hybridization. Additionally, the angles between carbon atoms stand at 159.80° and 160.19° (Fig. 3.1(a)). These structural findings align well with previous DFT studies (refer to Table 1) [25-26].

The HOMO and LUMO energies, determined as -8.51 eV and -1.77 eV respectively, yield a calculated HOMO-LUMO gap (E_G) of 6.74 eV using equation (1), consistent with prior research (see Table 1) [26]. The Fermi level energy (E_F), positioned between the HOMO and LUMO at -5.14 eV (equation 2), is visually represented by the HOMO and LUMO electron densities in Fig. 3.1(b and c). Our examination of the C_{18} nanocluster's charge distribution via Mulliken charge population analysis reveals distinctive positive and negative charge distributions among neighbouring carbon atoms (Fig. 3.1(d)).

The density of states (DOS) plot in Fig. 3.2 further supports our calculated HOMO, LUMO, and E_G values, corroborating the findings presented in Table 3.1.

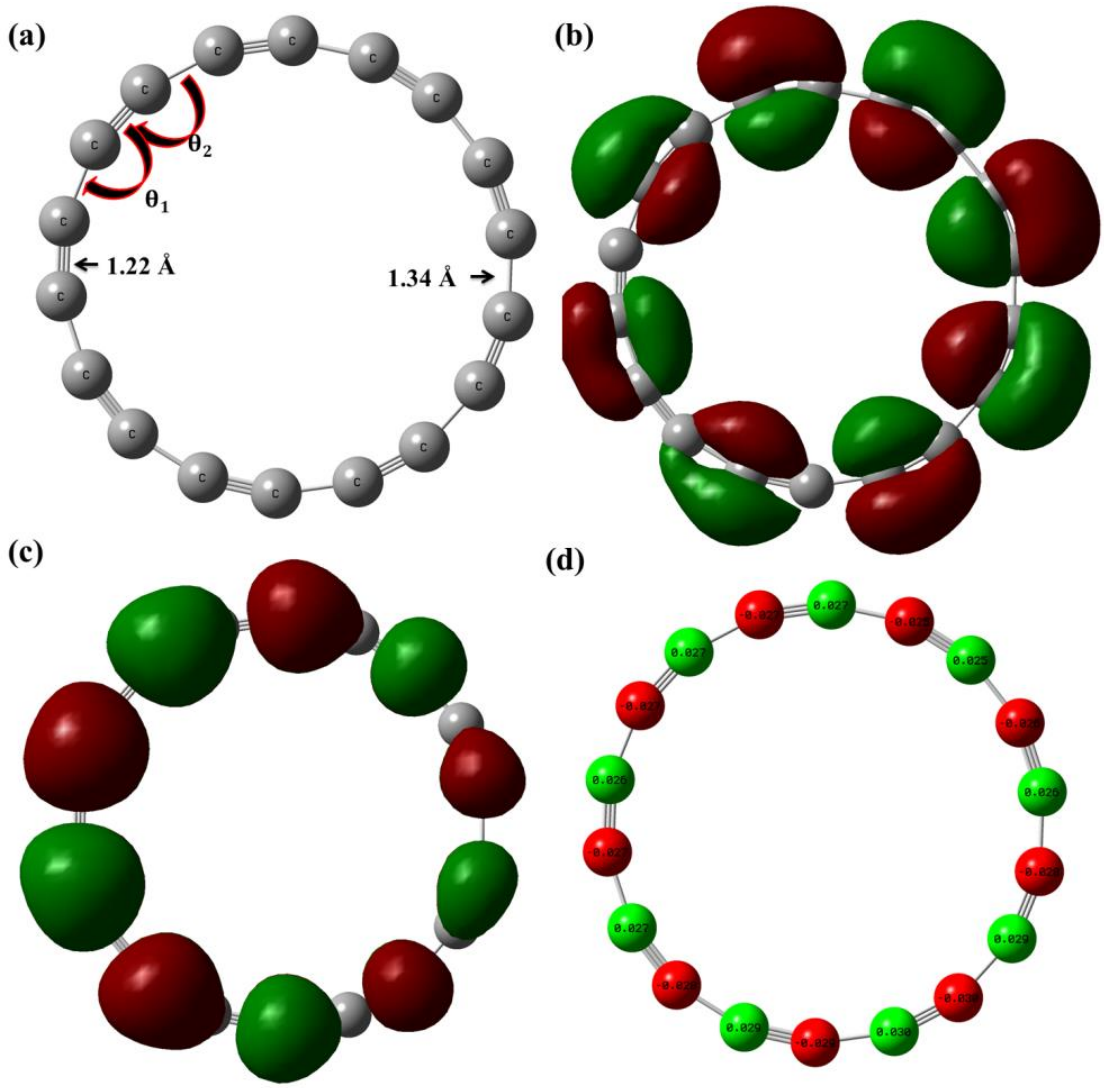

Figure 3.1: Optimized molecular structure (a), HOMO electron density (b), LUMO electron density (c) and Mulliken atomic charge distribution (d) of C_{18} nanocluster, respectively.

Table 3.1: Structural parameters, E_{HOMO} and E_{LUMO}, HOMO-LUMO gap (E_G) and dipole moment for C_{18} nanocluster.

System	Bond length (Å)		Angle (°)		E_{HOMO} (eV)	E_{LUMO} (eV)	E_G (eV)	Dipole moment (Debye)	Ref.
	C-C	C≡C	θ_1	θ_2					
C_{18}	1.34	1.22	160.19	159.80	-8.51	-1.77	6.74	0.000	Our work
	1.346	1.223	160.2	159.8	---	----	----	----	[25]
	---	----	----	----	-8.45	-1.70	6.75	----	[26]

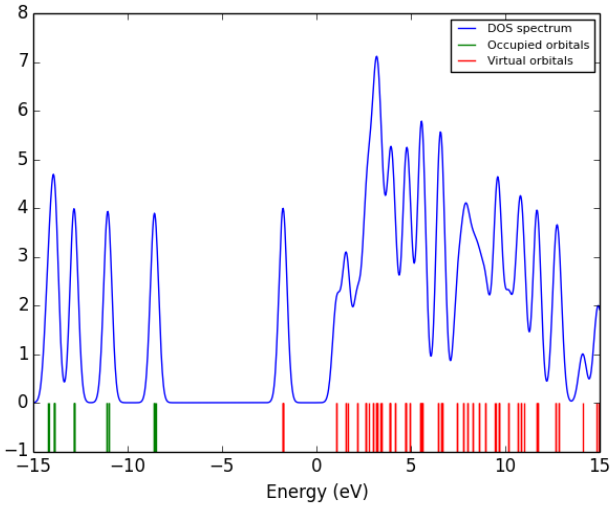

Figure 3.2: DOS spectrum for pristine C_{18} nanocluster.

3.3.2. Adsorption performance of CO, NO and NH_3 gas molecules adsorbed C_{18} nanocluster

Initially, we optimized the isolated CO, NO, and NH_3 gas molecules, analyzing their structural and vibrational characteristics and validating our findings by comparing them with existing reports. To understand how these gas molecules interact with the C_{18} nanocluster, we calculated the adsorption energy [36-42] using the following formula:

$$E_{ad} = E(C_{18}+Gas) - E(C_{18}) - E(Gas) + \delta_{BSSE} \text{ ----- (3a)}$$

This equation involves $E(C_{18}+Gas)$, indicating the total energy of the C_{18} nanocluster with the gas molecule adsorbed, $E(C_{18})$ representing the total energy of the pristine C_{18} nanocluster, E(Gas) denoting the total energy of the gas molecule in isolation, and δ_{BSSE} considering the energy correction due to basis set superposition error (BSSE). However, as we found the energy correction from BSSE to be insignificant, we've chosen to omit δ_{BSSE}. Thus, equation (3a) now simplifies to:

$$E_{ad} = E(C_{18}+Gas) - E(C_{18}) - E(Gas) \quad \text{----- (3b)}$$

For both CO and NO gases, we placed them at different sites on the C_{18} nanocluster, such as atop a carbon atom, a triple bond, and a single bond. Moreover, we explored various orientations for each gas molecule, considering the C/N or O head of CO/NO and a horizontal orientation at each site of the C_{18} nanocluster. As for NH_3 gas, we examined the N head, vertical, and three H head orientations at various locations on the C_{18} nanocluster. Among the different potential configurations for each gas molecule, we selected the most stable arrangement, specifically those configurations with the lowest energy, for subsequent calculations.

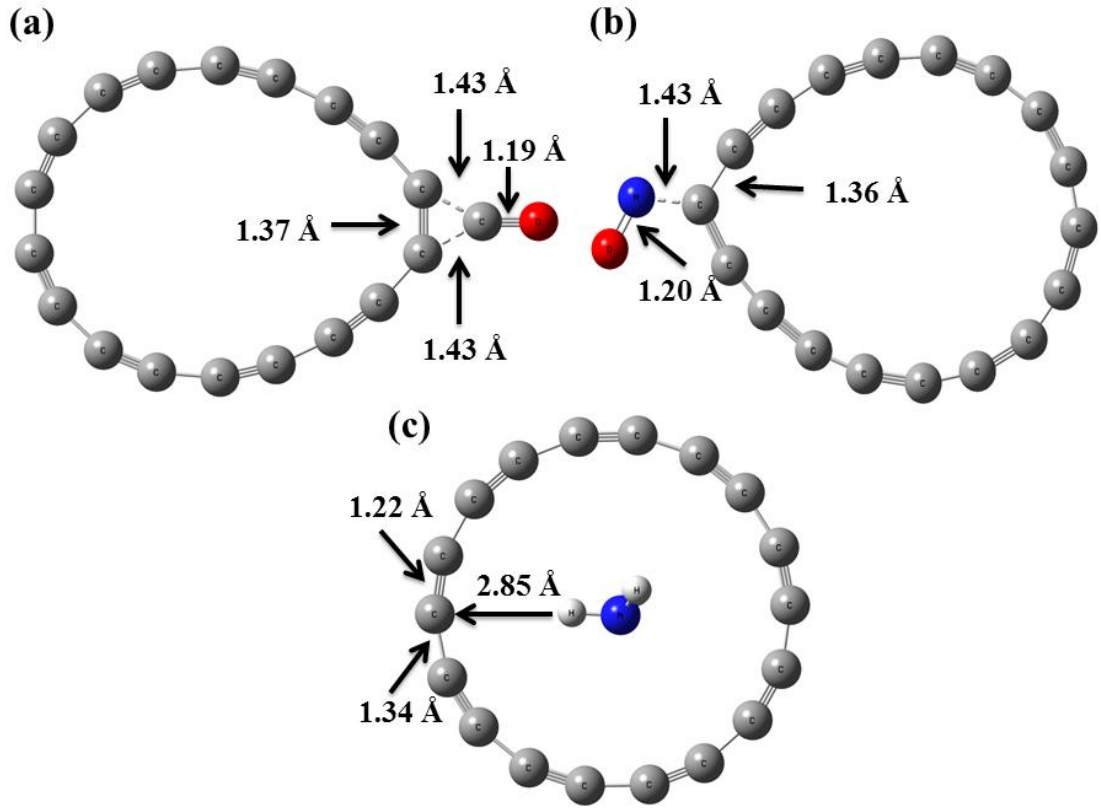

Figure 3.3: Stable-most configurations for the CO (a), NO (b) and NH_3 (c) adsorbed C_{18} nanoclusters

The computed adsorption energy for CO gas on the C_{18} nanocluster, using equation (3), stands at -0.31 eV. In Fig. 3(a), the configuration with the lowest energy for CO adsorption is presented. After CO gas adsorption, the C head of the CO molecule maintains a distance of 1.43 Å from the closest carbon atom of the C_{18} nanocluster. The interaction causes an increase in the bond length of the CO gas molecule from 1.12 Å to 1.19 Å (see Fig. 3.3(a)). Following adsorption, the carbon-carbon bond length extends from 1.22 Å to 1.37 Å, as depicted in Fig. 3.3(a). This close adsorption distance, coupled with the elongation of the carbon-carbon bond

length, indicates a chemisorptive interaction between the CO molecule and the C_{18} nanocluster. Fig. 3(b) displays the configuration with the least energy for NO adsorption, showcasing an adsorption energy of -0.29 eV for NO on the C_{18} nanocluster. After NO gas adsorption, the N head of the NO gas stays at a distance of 1.43 Å from the carbon atom of the C_{18} nanocluster. The bond length of the NO gas molecule increases from 1.14 Å to 1.20 Å post adsorption, depicted in Fig. 3(b). Simultaneously, the carbon-carbon bond length expands from 1.34 Å to 1.36 Å after NO adsorption. This change indicates a chemisorptive behaviour similar to that of the CO gas molecule over the C_{18} nanocluster. In Fig. 3(c), the lowest energy configuration for NH_3 adsorption on the C_{18} nanocluster reveals NH_3 gas molecules adsorbing at the hollow site, with an adsorption energy of -0.23 eV. The closest distance between the H atom of the NH_3 gas molecule and the carbon atom of the C_{18} nanocluster measures at 2.85 Å. The average N-H bond length of the NH_3 gas, remaining consistent at 1.01 Å, shows no change after adsorption, mirroring the isolated NH_3 gas molecule. Additionally, there are no alterations in the carbon-carbon bond lengths of the C_{18} nanocluster. The substantial adsorption distance and unchanged bond lengths suggest minimal interaction between the NH_3 gas molecule and the C_{18} nanocluster, indicating a physisorptive nature in NH_3 adsorption over the C_{18} nanocluster.

3.3.3. Electronic properties after the adsorption

The potential for charge transfer between the C_{18} nanocluster and gas molecules prompts an examination of the Mulliken atomic charge distribution [37, 43-44]. Post adsorption of CO, NO, and NH_3, the total Mulliken charge on the gas molecules registers as -0.76e, +0.07e, and -0.10e, respectively. This signifies a transfer of charge from the C_{18} nanocluster to CO and NH_3 gas molecules, as the isolated gas molecule holds a total Mulliken charge of zero. Conversely, in NO gas adsorption, the charge moves from the gas molecule to the C_{18} nanocluster [43-44]. Fig. 4 displays the charge distribution for the C_{18} nanocluster with adsorbed gas. Considering the electric dipole moment vector as an indicator of charge distribution [37, 43-44], the C_{18} nanocluster exhibits an even charge distribution, reflected in a dipole moment of 0.00 Debye. However, following the adsorption of CO, NO, and NH_3 gas molecules, the dipole moment shifts to 3.99 Debye, 4.23 Debye, and 0.43 Debye, respectively. These shifts in the dipole moment further affirm the alteration in charge distribution subsequent to gas adsorption in each instance.

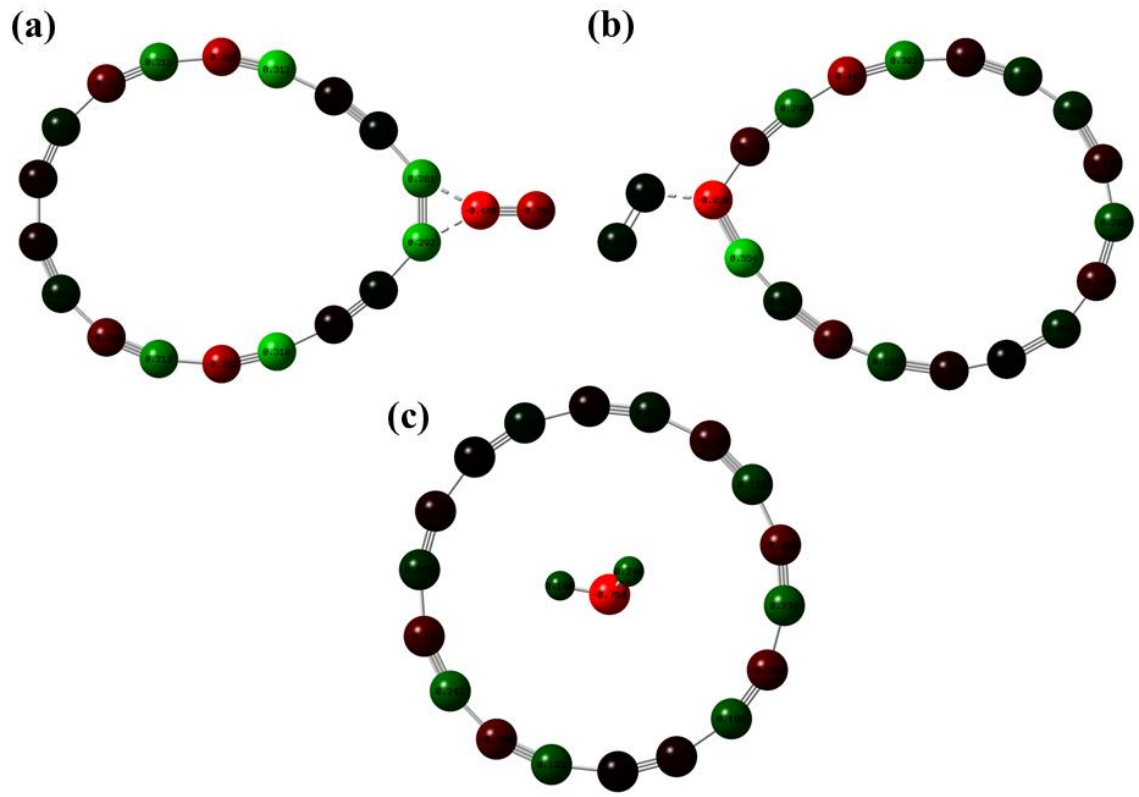

Figure 3.4: Mulliken charge population analysis of the CO (a), NO (b) and NH_3 (c) adsorbed C_{18} nanocluster, respectively.

For a thorough comprehension of the interplay between gas molecules and the C_{18} nanocluster, an array of parameters including HOMO, LUMO, E_F, ΔE_F, E_G, and ΔE_G were computed and are meticulously documented in Table 3.2 [37-44]. Furthermore, an in-depth examination of the density of states for the C_{18} nanocluster with adsorbed gas molecules was conducted, juxtaposed with the pristine C_{18} nanocluster (refer to Fig. 3.5) [37-44]. Post-CO adsorption, there is a 5.93% reduction in E_G compared to the pristine C_{18} nanocluster, in line with the observations extracted from the DOS spectrum (refer to Fig. 3.5(a)). The scrutiny of the DOS spectra and Table 3.2 reveals a discernible shift in the Fermi energy accompanied by a corresponding adjustment in the Fermi level. In the instance of NO adsorption, molecular orbitals (MOs) undergo a split into α-MOs and β-MOs (spin up and spin down). Subsequently, after CO and NO adsorption, there is a respective decline of 4.66% and 11.28(α)% (or 14.28(β)%) in the Fermi energy. Furthermore, α-E_G and β-E_G witness respective reductions of 21.66% and 14.68% in comparison to the pristine C_{18} nanocluster, as evident from the DOS spectrum (refer to Fig. 5(b)). Both Figs. 3.5(a) and 3.5(b) underscore an augmented contribution of DOS in the valence band, underscoring the chemisorptive nature of CO and NO gas molecules over the C_{18} nanocluster. In the case of NH_3 adsorption, while E_G also diminishes

by 5%, the shift in the DOS (refer to Fig. 3.5(c)) is marginal, indicating a physisorptive nature. Following NH_3 adsorption, there is a noteworthy elevation of 10.11% in the Fermi energy. Figs. 3.6 (a and b) illustrate the electron densities of HOMO and LUMO [37-44] after CO adsorption on the C_{18} nanocluster. These figures distinctly showcase the concentration of HOMO electron density on both the CO gas molecule and the region between the gas molecule and the C_{18} nanocluster. Additionally, the LUMO electron density localizes between the nearest carbon atom of the C_{18} nanocluster with adsorbed gas and its neighbouring carbon atom.

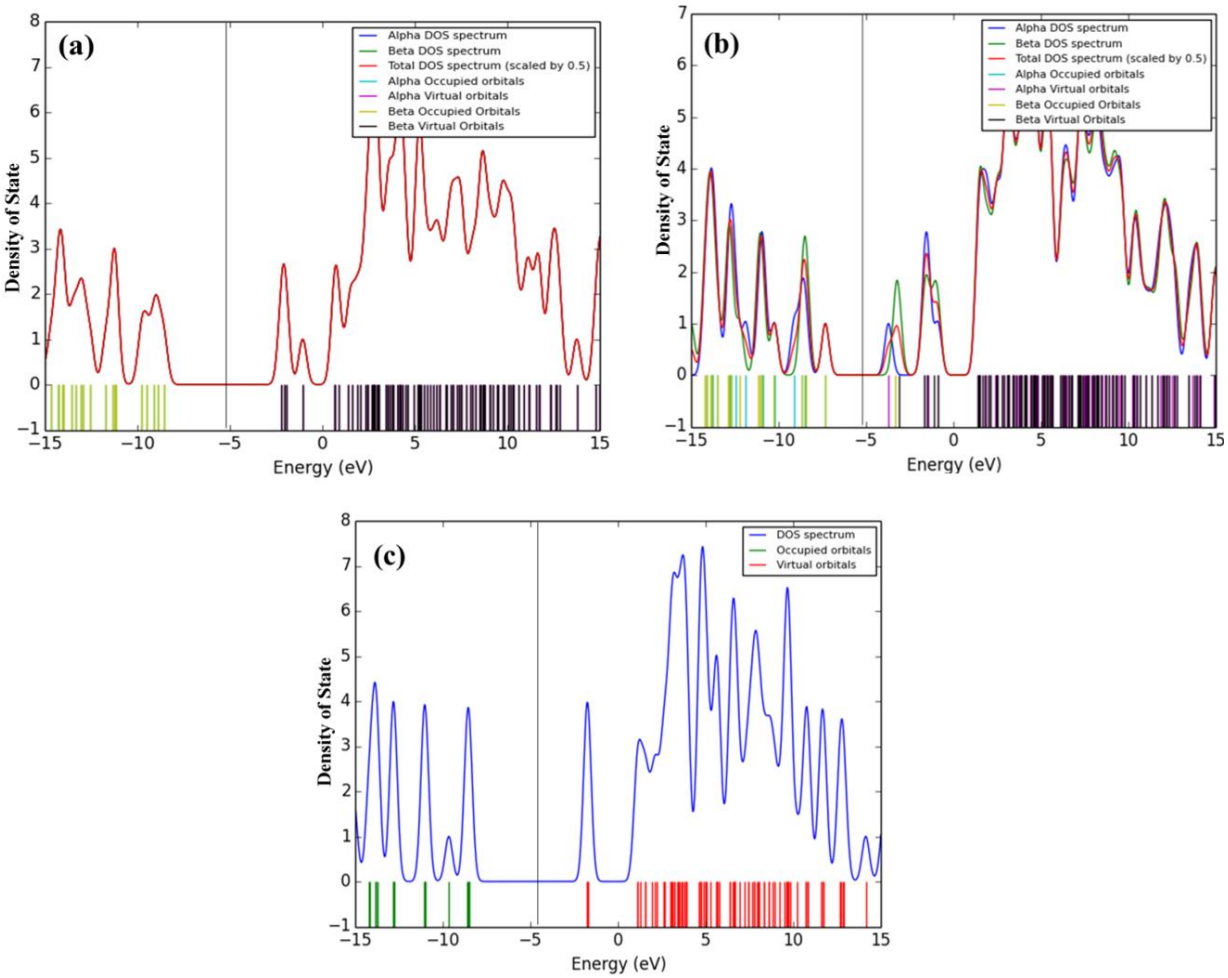

Figure 3.5: DOS spectra for CO (a), NO (b) and NH_3 (c) adsorbed C_{18} nanocluster, respectively.

Table 3.2: Adsorption energy (E_{ad}), HOMO and LUMO energies (E_{HOMO} and E_{LUMO}), HOMO-LUMO gap (E_G), change in E_G (ΔE_G), work function (φ), average adsorption distance (d) and dipole moment (D) of CO, NO and NH_3 adsorbed C_{18} nanoclusters, respectively.

System	E_{ad} (eV)	E_{HOMO} (eV)	E_F (eV)	ΔE_F (%)	E_{LUMO} (eV)	E_G (eV)	ΔE_G (%)	φ (eV)	d (Å)	D (Debye)
CO/C_{18}	-0.31	-8.55	-5.38	-4.66	-2.21	6.34	-5.93	5.38	1.43	3.99
NO/C_{18}	-0.29	-8.36^{α} -8.76^{β}	-5.72^{α} -5.88^{β}	-11.28^{α} -14.28^{β}	-3.08^{α} -3.01^{β}	5.28^{α} 5.75^{β}	-21.6 -14.7	5.72^{α} 5.88^{β}	1.43	4.23
NH_3/C_{18}	-0.23	-7.47	-4.62	+10.11	-1.77	5.69	-5.00	4.62	2.85	0.43

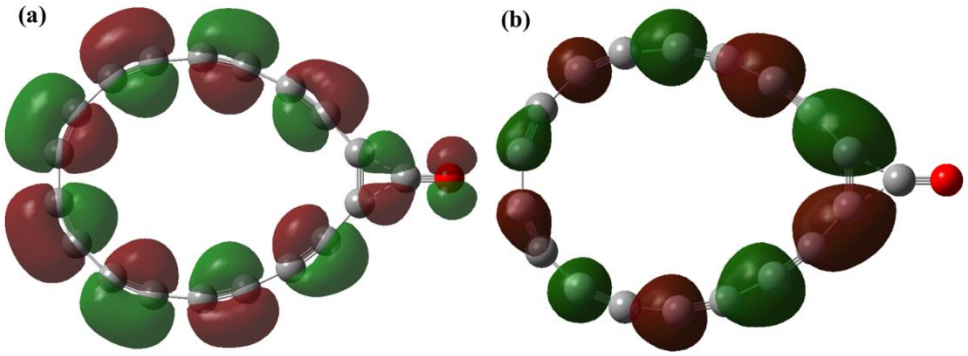

Figure 3.6: HOMO (a) and LUMO (b) electron density of CO adsorbed C_{18} nanocluster, respectively.

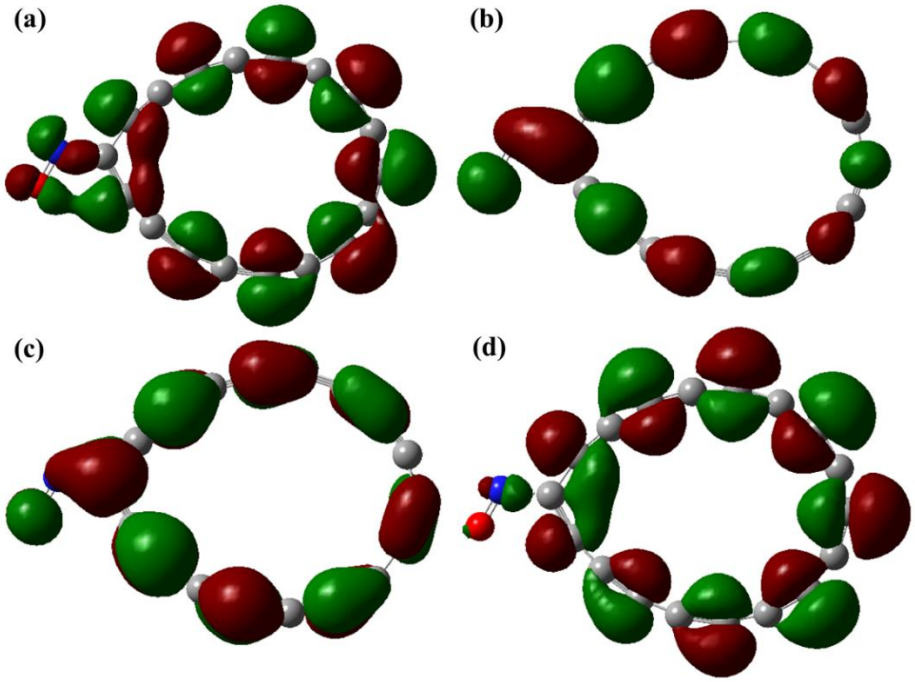

Figure 3.7: α-HOMO (a), α-LUMO (b), β-HOMO (c) and β-LUMO (d) electron density of NO adsorbed C_{18} nanocluster, respectively.

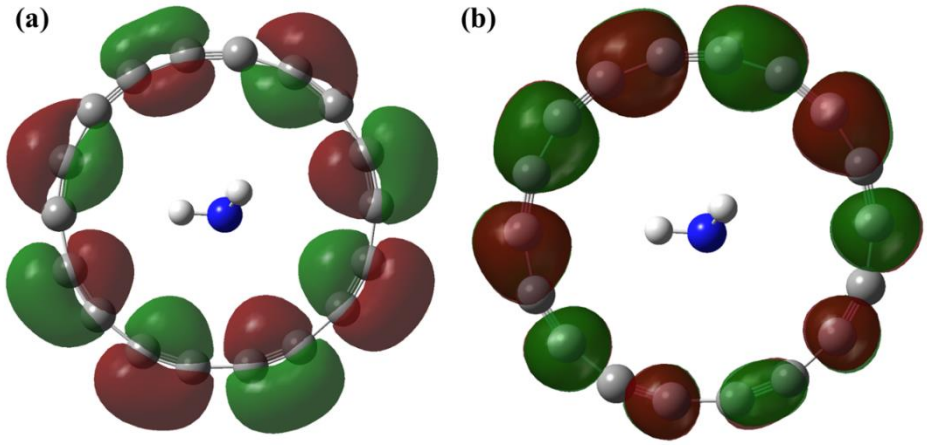

Figure 3.8: HOMO (a) and LUMO (b) electron density of NH_3 adsorbed C_{18} nanocluster, respectively.

In Figures 3.7(a, b, c, and d), we observe the α-HOMO, α-LUMO, β-HOMO, and β-LUMO electron densities for the C_{18} nanocluster with adsorbed NO. A notable observation is the concentration of α-HOMO and β-HOMO (refer to Figs. 3.7(a and c)) close to or between the NO gas molecule and the C_{18} nanocluster. Figures 3.7(b and d) distinctly show the concentration of both α-LUMO and β-LUMO between the NO gas molecule and the C_{18} nanocluster. This electron density concentration strongly supports the chemisorptive nature of CO and NO gas molecules over the C_{18} nanocluster. In the case of NH_3 adsorption, the absence of significant HOMO and LUMO electron densities (refer to Figs. 3.8(a and b)) over the NH_3 gas molecule, with minimal deviation from the pristine C_{18} nanocluster (refer to Figs. 1(b and c)), confirms the weak interaction.

3.3.4. Electrostatics potential (ESP) analysis

The Electrostatic Potential (ESP), an indicator of positive, neutral, and negative electrostatic potential regions, alongside molecular size and shape, is a valuable tool for understanding how gas molecules interact with the C_{18} nanocluster [37, 41-44]. Following convention, the blue, green, and red areas represent positive, neutral, and negative electrostatic potential regions. The red and blue zones signify electrophilic and nucleophilic activity, respectively, where positively charged particles bind strongly due to an excess of electrons and negatively charged particles bind strongly due to an electron deficiency. Fig. 9 displays the ESP surfaces of both the pristine C_{18} nanocluster and the C_{18} nanocluster with gas molecules adsorbed. The ESP of the pristine C_{18} nanocluster (refer to Fig. 3.9(a)) shows repetitive positive (blue region) and negative (yellow region) electrostatic potential areas, supporting Mulliken charge analysis.

After CO adsorption, evident negative electrostatic potential areas emerge near the O atom of the CO molecule, attributed to oxygen's higher electronegativity compared to carbon, consistent with the accumulation of negative Mulliken charge on the CO molecule post-adsorption (refer to Fig. 3.9(b)). Likewise, after NO adsorption, noticeable negative electrostatic potential regions appear near the O atom of the NO molecule due to oxygen's higher electronegativity compared to nitrogen (refer to Fig. 3.9(c)). Upon NH_3 adsorption, a negative electrostatic potential region is observed near the N atom of the NH_3 molecule, while positive electrostatic potential regions appear near the H atoms of NH_3, influenced by the higher electronegativity of the N atom in the NH_3 gas molecule (refer to Fig 9(d)). This observation aligns with the Mulliken charge analysis.

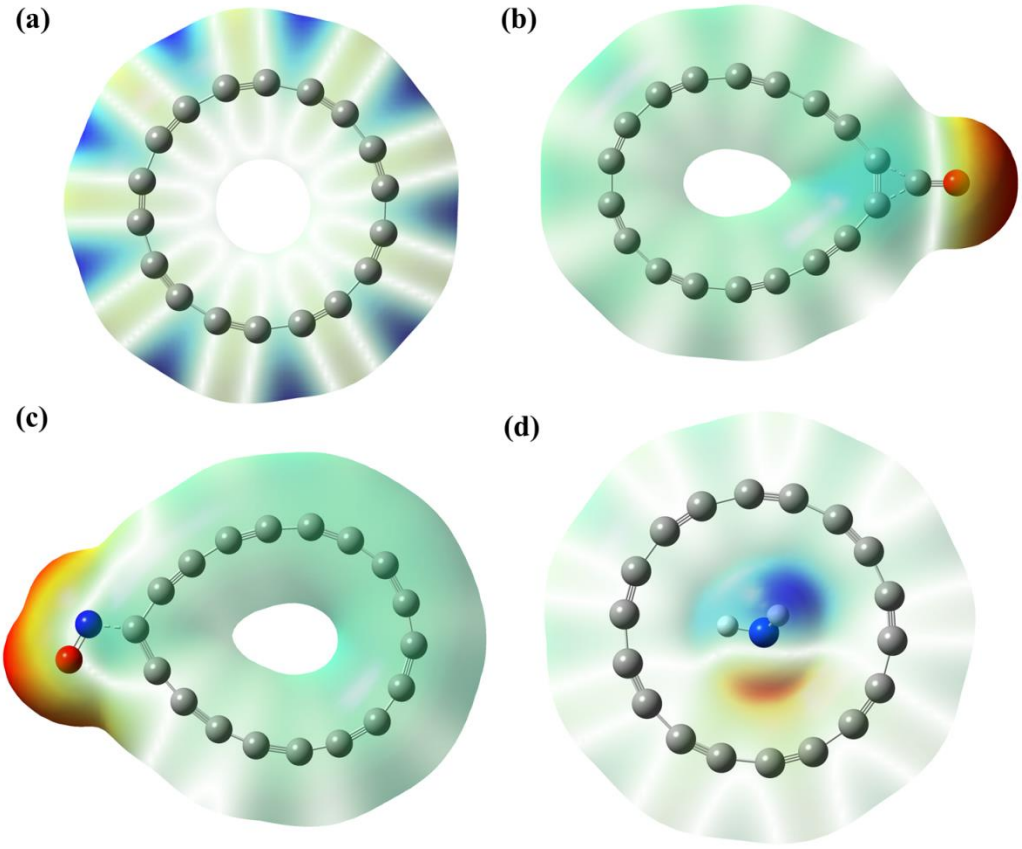

Figure 3.9: ESP maps of C_{18} nanocluster (a) and CO (b), NO (c) and NH_3 (d) adsorbed C_{18} nanocluster, respectively.

3.3.5. Sensing properties of C_{18} nanocluster

The sensing or sensitivity characteristics of the C_{18} nanocluster regarding the chosen gas molecules can be determined by examining the conductivity [37-38, 41], expressed by the following equation:

$$\sigma = AT^{3/2}\exp(\frac{-E_G}{2kT}) \text{ -----(4)}$$

In this equation, various symbols are defined: σ represents the electrical conductivity, A is a placeholder, E_G stands for the HOMO-LUMO gap, *k* denotes the Boltzmann constant, and T signifies the temperature. Equation (4) reveals an intriguing correlation at a given temperature—electrical conductivity and E_G share an inverse relationship. This implies that as E_G decreases, the electrical conductivity tends to rise, as evidenced in Table 2. When exposed to CO, NO, and NH_3, the C_{18} nanocluster undergoes a noticeable increase in conductivity, directly linked to the decrease in E_G. As E_G reduces, the resistance of the C_{18} nanocluster diminishes. These changes in material resistance are proportionate to the concentration of gas molecules present in the environment. The significant impact of gas molecules on the C_{18} nanocluster's electronic properties hints at its potential as an electronic sensor for gas detection.

In the realm of gas molecule sensors, the recovery time holds paramount importance [2, 43-45]. It defines the expected duration until the adsorbed molecule detaches from its hosting system. For an efficient gas sensor, shorter recovery times are preferable. A strong interaction between gas molecules and the sensor hampers the desorption process, leading to prolonged recovery times. The recovery time [2, 43-45] is calculated as follows:

$$\tau = \upsilon^{-1}\exp(\frac{-E_{ad}}{kT}) \text{ -----(5)}$$

The formula provided employs symbols where τ signifies the recovery time, υ represents the attempt frequency, E_{ad} stands for adsorption energy, k is the Boltzmann constant, and T denotes the temperature. To establish a more comprehensive analysis of recovery times, three distinct attempt frequencies (υ) have been utilized—$1x10^{12}$ Hz (infrared), $5.2x10^{14}$ Hz (yellow light), and $1x10^{16}$ Hz (UV light)—coupled with two different temperatures (T = 300 K and T = 500 K) [2, 43-45]. Recovery times denoted as τ_I, τ_Y, and τ_U for infrared, yellow, and UV light, respectively, have been computed. The determined recovery times (using equation 5) for CO and NO adsorption vary from nanoseconds (ns) to picoseconds (ps) and even femtoseconds (fs) across different frequencies and temperatures (refer to Table 3.3). These calculated times indicate remarkably swift desorption processes for CO and NO gas molecules. Such swift recovery times position C_{18} nanoclusters as highly promising options for CO and NO sensor applications. However, despite the very short recovery time for NH_3 adsorption, its physisorptive nature suggests it might not be suitable for sensor applications.

Table 3.3: Calculated recovery time (τ_I, τ_Y and τ_U) of CO, NO and NH_3 adsorbed C_{18} nanoclusters at T = 300 K and T = 500K, respectively.

System	τ_I		τ_Y		τ_U	
	T= 300 K	T = 500K	T= 300 K	T = 500 K	T = 300K	T = 500K
CO/C_{18}	162.70 ns	1.33 ns	0.31 ns	2.57 ps	16.27 ps	133.90 fs
NO/C_{18}	74.60 ns	0.83 ns	0.14 ns	1.60 ps	7.46 ps	83.70 fs
NH_3/C_{18}	7.31 ns	0.20 ns	0.01 ns	0.40 ps	0.73 ps	20.80 fs

Gas adsorptions significantly impact the Fermi level and work function (φ) of materials, which are critical factors for a φ-type sensor. In φ-type sensors, the Kelvin theory of oscillators is employed to estimate the φ values before and after the gas molecule interaction [37]. When the gas interaction causes increase or decrease in the sensor's φ, it disrupts the gate voltage, resulting in the generation of an electrical signal [34]. The work function (φ) is formally described as the minimum energy needed to extract an electron from a material to a location just outside the solid surface, as represented by the following equation [36, 38].

$$\varphi = V_{el(+\alpha)} - E_F \text{ -----(6)}$$

Here, $V_{el}(+\alpha)$ represents the electrostatic potential energy at a distance from the material surface, and E_F denotes the Fermi energy. According to equation (6), when $V_{el}(+\alpha)$ equals zero, we can express φ as $-E_F$. The alteration in the φ value of an adsorbent system during the gas adsorption process impacts its field emission characteristics, and this relationship can be linked through the classical Richardson-Dushman equation [36, 38]. The current density of emitted electrons in a vacuum is determined by the Richardson-Dushman equation.

$$j = AT^2\exp(-\varphi/kT) \text{ -----(7)}$$

Here, A represents the Richardson constant (A/m^2), and T stands for temperature. Following gas adsorption, the interaction between gas molecules and the C_{18} nanocluster leads to a modification in the Highest Occupied Molecular Orbital (HOMO) and Lowest Unoccupied Molecular Orbital (LUMO) energies of the C_{18} nanocluster. This alteration in HOMO and LUMO energies subsequently results in changes to the work function and Fermi energy, as detailed in Table 2. The work function experiences a positive increase of +4.66% and +11.28(α)% (or +14.28(β)%) attributed to a shift in the LUMO energy magnitude from -1.77 eV to -2.21 eV and -3.08(α) eV (or -3.01(β) eV) during CO and NO adsorption, respectively. Conversely, in the case of NH_3 adsorption, there is a decrease of -10.11% in φ due to a change in the HOMO energy from -8.45 eV to -7.47 eV. Our findings indicate that the C_{18} nanocluster can serve as a sensitive φ sensor for NH_3 gas molecules, as the maximum change in φ is

observed compared to the change in E_G. However, it's important to note that NH_3 gas molecules exhibit physisorption, indicating that the C_{18} nanocluster may not be suitable for sensor applications in this context.

3.3.6. Absorption and Raman spectra

The absorption characteristics for both before and after gas interaction of C_{18} nanoclusters are examined using TDDFT-ωB97XD/6-311++G(d, p) at their respective ground-state geometries, as indicated in Fig. 10. An evident absorption peak, approximately at 220.00 nm, corresponds to an E_G value of 6.74 eV for the pristine C_{18} nanocluster, consistent with an earlier DFT investigation (see Fig. 3.10(a)) [26]. Upon CO adsorption, the absorption peak slightly shifts to around 215 nm, reflecting the reduced E_G of 6.34 eV (see Fig. 3.10(b)). Conversely, NH_3 adsorption leads to an absorption peak at 223.00 nm, aligning with a lower E_G of 5.69 eV (see Fig. 3.10(d)). However, for the C_{18} nanocluster with NO adsorption, the detected absorption peaks at 300.00 nm and 384.00 nm, attributed to α-LUMO and β-LUMO, respectively, appear weaker compared to the peaks observed in C_{18}, CO, and NH_3 adsorbed C_{18} nanocluster (refer to Fig. 3.10(c)).

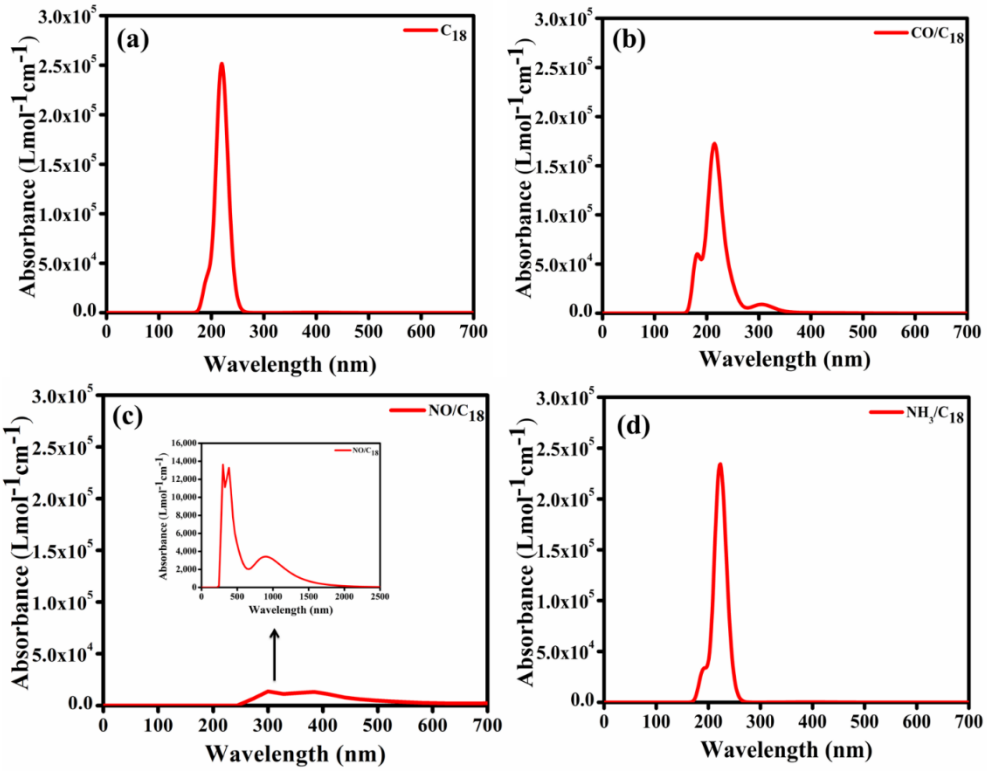

Figure 3.10: Absorption spectra for pristine (a) and CO (b), NO (c) and NH_3 (d) adsorbed C_{18}

Raman spectroscopy is a good experimental method to study materials without causing damage. It not only helps us understand material properties but also sheds light on how gas molecules interact with the materials. Techniques like in situ spectroscopy, including Raman spectroscopy, let us assess the gas composition and qualitatively analyze how these gases interact with the material [46-49]. In this study, we examined Raman spectra for both the pristine C_{18} nanocluster and the same cluster exposed to different gases (see Fig. 11). These spectra offer valuable information about the types of bonds and functional groups within the material. Vibrational frequencies reflected as Raman shifts depend on atomic masses and bond strengths. We employed the CAM-B3LYP/6-311+G(d,p) level of theory for Raman spectrum calculations [47].

For example, we found that the 898.50 cm^{-1} band corresponds to the weak C-C bond, while the bands at 1765.50 cm^{-1} and 2188.00 cm^{-1} represent strong C≡C bonds (see Fig. 3.11(a)) [47]. Changes or new bands in the spectrum usually indicate the interaction between gas molecules and the C_{18} nanocluster. In our analysis, we observed new weak bands and a shift in another weak band, particularly at 827.00 cm^{-1} and 941.00 cm^{-1}. This alteration suggests that the interaction between CO gas molecules and one of the C≡C bonds influences specific weak bands. Moreover, vibrations at 1565.00 cm^{-1} and the presence of three strong C≡C bonds imply a change in the overall symmetry of the ring due to this interaction. Additionally, the intense peak at 2024.00 cm^{-1} confirms the presence of CO gas molecules (refer to Fig. 3.11(b)) [48]. This underlines a strong covalent interaction with the C_{18} nanocluster, corroborating previous findings on adsorption energy.

For NO-adsorbed C_{18} nanoclusters, new bands in both weak (C-C) and strong (C≡C) bonds suggest increased bond strength compared to the pristine nanocluster. This signifies a more significant distortion due to symmetry breaking, far more noticeable than in both the pristine and CO-adsorbed C_{18} nanoclusters. Our analysis hints at a covalent bond nature, supported by the appearance of the NO Raman band at 1869.00 cm^{-1} (see Fig. 3.11(c)), consistent with earlier studies on NO gas [48]. However, in NH_3-adsorbed C_{18} nanoclusters, a red shift in C≡C Raman bands implies electron loss from the C_{18} nanocluster to NH_3. Importantly, the absence of NH_3 in the Raman spectra (see Fig. 11(d)) supports physisorption, consistent with previous findings [49]. Conversely, the presence of CO and NO peaks confirms the chemisorption nature of their interaction with the C_{18} nanocluster.

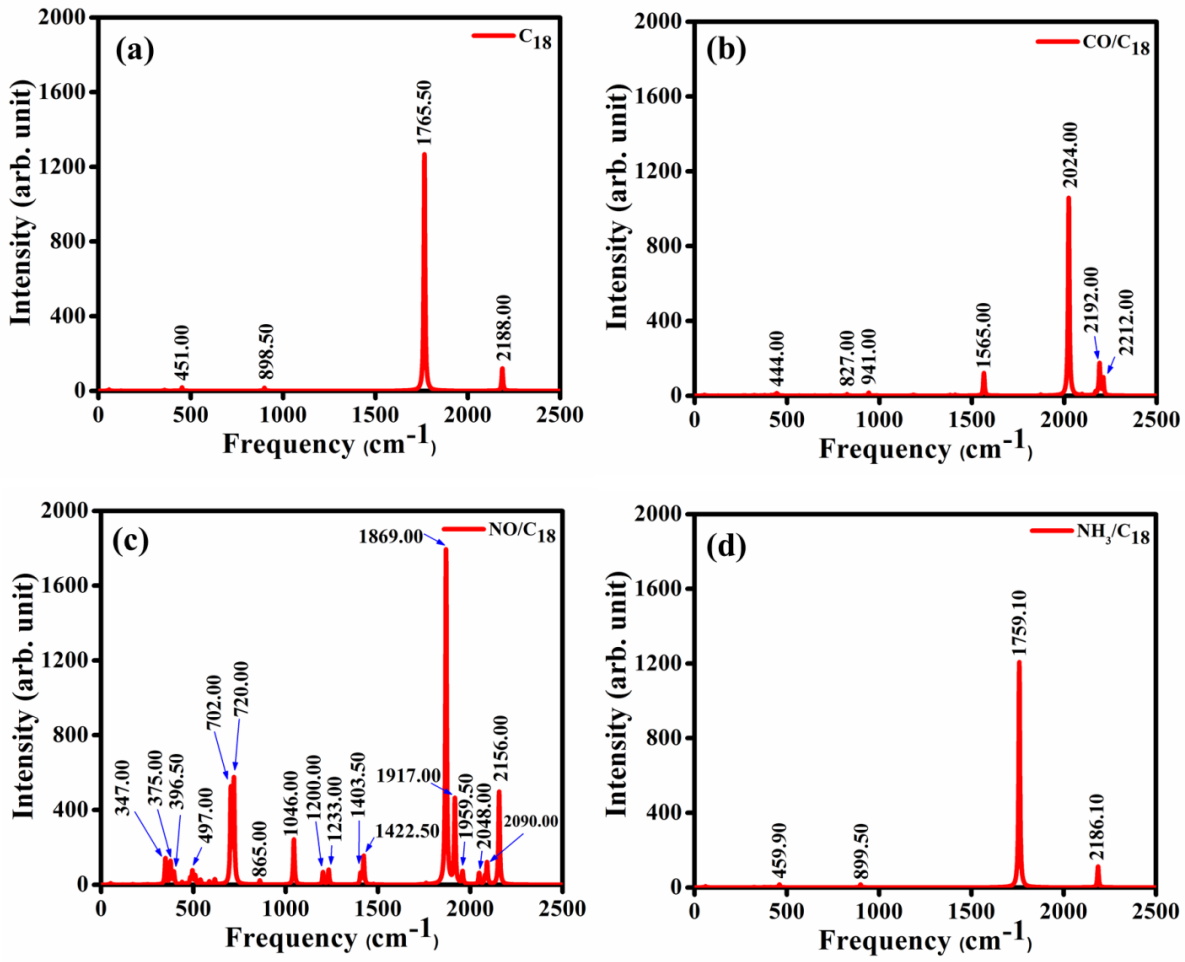

Figure 3.11: Raman spectra of pristine (a) and CO (b), NO (c) and NH_3 (d) adsorbed C_{18} nanocluster, respectively.

3.3.7. Global reactivity indices

The investigation of the activity of clusters or molecular systems involves the calculation of global indices parameters [37, 43], including chemical potential (μ), softness (S), hardness (η), and electrophilicity (ω). These global indices parameters are determined by the following formulas,

$$\text{Chemical Potential } (\mu) = -\frac{I+A}{2} \text{-----(8)}$$

$$\text{Hardness } (\eta) = \frac{I-A}{2} \text{-----(9)}$$

$$\text{Softness } (S) = \frac{1}{2\eta} \text{-----(10)}$$

$$\text{Electrophilicity } (\omega) = \frac{\mu^2}{2\eta} \text{-----(11)}$$

Here, I ≅ - E_{HOMO} and A ≅ - E_{LUMO}. The tabulated global indices parameters, calculated using equations (8) to (11), are presented in Table 3.4.

Table 3.4: Chemical potential (μ), hardness (η), softness (S) and electrophilicity (ω) for CO, NO and NH_3 adsorbed C_{18} nanoclusters, respectively.

System	μ (eV)	η (eV)	S $(eV)^{-1}$	ω (eV)
C_{18}	-5.14	3.37	0.14	3.91
CO/C_{18}	-5.38	3.17	0.15	4.56
NO/C_{18}	-5.72^{α}	2.64^{α}	0.18^{α}	6.19^{α}
	-5.88^{β}	2.87^{β}	0.17^{β}	6.02^{β}
NH_3/C_{18}	-4.62	2.85	0.17	3.74

The chemical potential (μ) of the pristine C_{18} nanocluster stands at -5.14 eV. However, upon gas adsorption, there are substantial shifts in μ due to changes in the HOMO and LUMO positions within the systems. Specifically, the μ values experience variations of +4.66%, +11.28(α)% (or +14.39(β)%), and -10.11% for C_{18} nanoclusters adsorbed with CO, NO, and NH_3, respectively. Compared to the pristine C_{18} nanocluster, the chemical potential is highest in NH_3 adsorption and lowest in NO adsorption. The system's chemical stability, as measured by hardness (η) at 3.37 eV for the C_{18} nanocluster, diminishes after CO, NO, and NH_3 adsorption, decreasing by -5.93%, -15.43(α)% (or -21.66(β)%), and -14.83%, respectively. This decline is attributed to the reduction in E_G post-gas adsorption.

Conversely, softness (S), inversely related to hardness, increases as the hardness of the gas-adsorbed system decreases. The softness values listed in Table 4 follow the sequence C_{18} < CO/C_{18} < NH_3/C_{18} = NO/C_{18} (β) < NO/C_{18} (α). For CO, NO, and NH_3 gas adsorption, softness escalates by +7.14%, 28.57(α)% (or 21.42(β)%), and 21.42%, respectively, in comparison to the pristine C_{18} nanocluster. Electrophilicity (ω), indicating the tendency to accept electrons from atoms or molecules, is measured at 3.91 eV for the pristine C_{18} nanocluster. This electrophilicity surges by +16.62% and 58.31(α)% (or 53.96(β)%) for CO and NO adsorption, respectively, and diminishes by -4.34% for NH_3 adsorption. Notably, electrophilicity peaks with NO gas adsorption and decreases notably with NH_3 gas adsorption.

3.3.8. C_{18} nanocluster as compared to other carbon nanomaterials

To assess the superiority of the pristine C_{18} nanocluster in terms of gas sensing, we compared the adsorption energy (E_{ad}) and adsorption distance (d) of toxic gas molecules CO, NO, and NH_3 on the C_{18} nanocluster with previously reported novel carbon-based nanomaterials [5-16]. Table 3.5 clearly indicates that CO, NO, and NH_3 gas molecules exhibit physisorption nature on various carbon-based nanomaterials, including graphene, single-walled carbon nanotubes (SWCNT), armchair graphene nanoribbon (AGNR), zigzag graphene nanoribbon (ZGNR), graphene quantum dot (GQD), and graphyne.

Table 3.5: Comparison of CO, NO and NH_3 gas adsorption properties of C_{18} nanocluster with other carbon based nanomaterials

System	CO			NO			NH_3		
	E_{ad} (eV)	d (Å)	Ref.	E_{ad} (eV)	d (Å)	Ref.	E_{ad} (eV)	d (Å)	Ref.
C_{18}	-0.31	1.43	Our work	-0.29	1.43	Our work	-0.23	2.94	Our work
Graphene	-0.01	3.85	[5]	-0.07	----	[6]	0.11	----	[7]
SWCNT	0.25	2.83	[8]	-0.09	2.88	[9]	-0.03	3.41	[10]
AGNR	-0.06	3.40	[11]	-0.13	3.32	[11]	-0.15	2.80	[12]
ZGNR	-0.09	----	[13]	-0.27	2.88	[14]	-0.09	3.03	[14]
GQD	-0.12	3.20	[15]	----	----	----	-0.11	2.87	[15]
Graphyne	-0.11	3.30	[16]	-0.12	3.15	[16]	-0.14	2.70	[16]

The poor adsorption energy and large adsorption distance from the surface of these materials imply that their pristine forms are not suitable for gas sensing purposes [5-16]. Contrastingly, our findings reveal that CO and NO gas molecules undergo chemisorption on the C_{18} nanocluster, exhibiting notably favourable adsorption energy and very short adsorption distances compared to the carbon-based nanomaterials mentioned in Table 5. Moreover, the adsorption energy of NH_3 over the C_{18} nanocluster is favourable compared to the mentioned carbon-based nanomaterials. However, the large adsorption distance suggests a weak interaction between NH_3 and the C_{18} nanocluster, indicating its unsuitability for gas sensing purposes. In summary, the C_{18} nanocluster emerges as an excellent candidate for CO and NO gas molecule sensing applications but not for NH_3 gas molecules.

3.4. CONCLUSION

In this chapter, we conducted an extensive investigation into the structural, electronic, vibrational, and adsorption properties of toxic gas molecules onto the C_{18} nanocluster using Density Functional Theory (DFT). The stability of the C_{18}, confirmed by its negative formation energy and absence of imaginary frequencies in the Raman and IR plots, supports its structural and dynamic robustness, validating the experimental realization of polyynic cyclo[18]carbon. The short adsorption distances (1.43 Å and 1.43 Å) and low adsorption energies (-0.31 eV and -0.29 eV) between CO and NO gas molecules and the C_{18} nanocluster indicate a chemisorption phenomenon. Conversely, the notably longer adsorption distance (2.85 Å) observed for NH_3 gas molecule adsorption suggests its physisorption behavior on the C_{18} nanocluster.

A transfer of charges, from the C_{18} to CO and NH_3 gas molecules (-0.76e and -0.10e, respectively) and from the NO gas molecule to the C_{18} nanocluster (+0.07e), leads to dipole moments ranging from 0 Debye to 3.99 Debye, 4.23 Debye, and 0.43 Debye for CO, NO, and NH_3 gas molecule adsorbed C_{18} nanoclusters, respectively. The reduction in the HOMO-LUMO gap from 6.74 eV to 6.34 eV, 5.28(α) eV (or 5.75(β) eV), and 5.69 eV following CO, NO, and NH_3 adsorption indicates a qualitative increase in electrical conductivity. This suggests the potential of the C_{18} nanocluster as a gas sensor for detecting these molecules.

The concentration of HOMO and LUMO electron densities near the CO and NO gas molecules aligns with their chemisorption behavior, while their absence near the NH_3 gas molecule supports physisorption. The theoretically calculated short recovery time for CO and NO gas molecules indicates the potential applicability of the C_{18} nanocluster as an 'ultra-fast gas sensor.' However, despite its short recovery time for NH_3 gas molecules and physisorption behavior, its practical utility might be limited. The evaluation of the adsorption capabilities of these gas molecules on the C_{18} nanocluster positions cyclo[18]carbon as a promising material in the domain of gas sensors when compared with other pristine carbon-based nanomaterials.

BIBLIOGRAPHY:

[1] D. Chodvadiya, N. N. Som, P. K. Jha and B. Chakraborty, *Int. J. Hydrogen Energy*, 2021, **46**, 22478–22498.

[2] D. Pandey, C. Kamal, R. Dutt and A. Chakrabarti, *Appl. Surf. Sci.*, 2020, **531**, 147364.

[3] Z. Cui, X. Wang, Y. Ding, E. Li, K. Bai, J. Zheng and T. Liu, *Appl. Surf. Sci.*, 2020, **530**, 147275.

[4] D. Upadhyay, B. Roondhe, A. Pratap and P. K. Jha, *Appl. Surf. Sci.*, 2019, **476**, 198–

204.

[5] W. Wang, Y. Zhang, C. Shen and Y. Chai, *AIP Adv.*, 2016, **6**, 025317.

[6] H. P. Zhang, X. G. Luo, X. Y. Lin, X. Lu, Y. Leng and H. T. Song, *Appl. Surf. Sci.*, 2013, **283**, 559–565.

[7] Y. Peng and J. Li, *Front. Environ. Sci. Eng.*, 2013, **7**, 403–411.

[8] R. Wang, D. Zhang, W. Sun, Z. Han and C. Liu, *J. Mol. Struct. THEOCHEM*, 2007, **806**, 93–97.

[9] X. Jia, L. An and T. Chen, *Adsorption*, 2020, **26**, 587–595.

[10] P. Buasaeng, W. Rakrai, B. Wanno and C. Tabtimsai, *Appl. Surf. Sci.*, 2017, **400**, 506–514.

[11] S. Kumar, M. Malhotra and H. Sharma, *Mater. Res. Express*, 2018, **5**, 105007.

[12] N. T. Cuong and N. M. Tien, *First-principles Studies of CO_2 and NH_3 Gas Molecules Adsorbed on Graphene Nanoribbons*, 2016, vol. 32.

[13] S. Kumar, Meenakshi and H. Sharma, in *Materials Today: Proceedings*, Elsevier Ltd, 2017, **4**, 10441–10445.

[14] E. Salih and A. I. Ayesh, *Sensors (Switzerland)*, 2020, **20**, 1–18.

[15] F. Montejo-Alvaro, J. Oliva, M. Herrera-Trejo, H. M. Hdz-García and A. I. Mtz-Enriquez, *Theor. Chem. Acc.*, 2019, **138**, 37.

[16] Z. Lu, P. Lv, D. Ma, X. Yang, S. Li and Z. Yang, *J. Phys. D. Appl. Phys.*, 2018, **51** 065109.

[17] B. Roondhe, K. Patel and P. K. Jha, *Appl. Surf. Sci.*, 2019, **496**, 143685.

[18] C. Jin, X. Tang, X. Tan, S. C. Smith, Y. Dai and L. Kou, *J. Mater. Chem. A*, 2019, **7**, 1099–1106.

[19] D. Ma, W. Ju, T. Li, X. Zhang, C. He, B. Ma, Z. Lu and Z. Yang, *Appl. Surf. Sci.*, 2016, **383**, 98–105.

[20] H. Cui, G. Zhang, X. Zhang and J. Tang, *Nanoscale Adv.*, 2019, **1**, 772–780.

[21] P. Li, Q. Hong, T. Wu and H. Cui, *Mol. Phys.*, 2021, **119**, e1919774.

[22] S. Arulmozhiraja and T. Ohno, *J. Chem. Phys.,* 2021, **128**, 114301.

[23] M. Z. Rahman and T. Edvinsson, *J. Mater. Chem. A*, 2020, **8**, 8234–8237.

[24] K. Kaiser, L. M. Scriven, F. Schulz, P. Gawel, L. Gross and H. L. Anderson, *Science (80-.).*, 2019, **365**, 1299–1301.

[25] N. D. Charistos and A. Muñoz-Castro, *Phys. Chem. Chem. Phys.*, 2020, **22**, 9240–9249.

[26] Z. Liu, T. Lu and Q. Chen, *Carbon N. Y.*, 2020, **165**, 461–467.

[27] A. J. Stasyuk, O. A. Stasyuk, M. Solà and A. A. Voityuk, *Chem. Commun.*, 2020, **56**, 352–355.

[28] S. Fang and Y. H. Hu, *Carbon N. Y.*, 2021, **171**, 96–103.

[29] G. Schatz, 2013.

[30] J. Da Chai and M. Head-Gordon, *Phys. Chem. Chem. Phys.*, 2008, **10**, 6615–6620.

[31] W. Kohn, A. D. Becke and R. G. Parr, *J. Phys. Chem.*, 1996, **100**, 12974–12980.

[32] K. M. L. Noel M. O'boyle, Adam L. Tenderholt, *J. Comput. Chem.*, 2008, **29**, 839–845.

[33] N. Sheikhsoleimani, M. Rouhani and H. Saeidian, *Inorg. Chem. Commun.*, 2020, **118**, 107997.

[34] M. A. Hossain, M. R. Hossain, M. K. Hossain, J. I. Khandaker, F. Ahmed, T. Ferdous and M. A. Hossain, *Chem. Phys. Lett.*, 2020, **754**, 137701.

[35] Y. Liu, C. Liu and A. Kumar, *Mol. Phys.*, 2020, **118**, 1–8.

[36] K. Sohlberg and N. Vedova-Brook, *J. Comput. Theor. Nanosci.*, 2004, **1**, 256–260.

[37] M. F. Fellah, *J. Phys. Chem. C*, 2011, **115**, 1940–1951.

[38] S. Demir and M. F. Fellah, *Surf. Sci.*, 2020, **701**, 121689.

[39] H. Y. Ammar, H. M. Badran and K. M. Eid, *Mater. Today Commun.*, 2020, **25**, 101681.

[40] S. Demir and M. F. Fellah, *Appl. Surf. Sci.*, 2020, **504**, 144141.

[41] R. Chandiramouli, A. Srivastava and V. Nagarajan, *Appl. Surf. Sci.*, 2015, **351**, 662–672.

[42] D. Paul, A. Vaidyanathan, U. Sarkar and B. Chakraborty, *Struct. Chem.*, 2021, **32**, 2259–2270.

[43] V. Sharma, N. N. Som, S. B. Pillai and P. K. Jha, *Spectrochim. Acta - Part A Mol. Biomol. Spectrosc.*, 2020, **224**, 2020–2023.

[44] S. Hussain, H. Chen, Z. Zhang and H. Zheng, *Chem. Commun.*, 2020, **56**, 2336–2339.

[45] Bhagavantam S, *Radiology*, 1932, **19**, 66–66.

[46] A. A. Akande, A. G. J. Machatine, B. Masina, G. Chimowa, B. Matsoso, K. Roro, M. M. Duvenhage, H. Swart, J. Bandyopadhyay, S. S. Ray and B. W. Mwakikunga, *J. Phys. D. Appl. Phys.*, 2017, **51**, 015106.